Supplementary Information for
Ultra-Wide Field-of-View Integrated Optical Phased Array Employing Multiple Orbital Angular Momentum Beams

Zhen Wang,[a] Shuxin Liu,[a] Jingchi Li,[a] Yong Zhang,[a] Xinyuan Fang,[b] Qiwen Zhan,[c] and Yikai Su [a,*]

[a] Shanghai Jiao Tong University, Department of Electronic Engineering and Electrical Engineering, Shanghai, China, 200240

[b] University of Shanghai for Science and Technology, School of Artificial Intelligence Science and Technology, Shanghai, China, 200093

[c] University of Shanghai for Science and Technology, School of Optical-Electrical and Computer Engineering, Shanghai, China, 200093

***** Yikai Su**,** E-mail: yikaisu@sjtu.edu.cn

S1 Design and optimization of the surface-emitting 1×3 Dammann grating

In the main text, the number of diffraction orders in a grating is determined by the ratio between its period and the Bragg period ($\Lambda_{Bragg} = \lambda/2n_{eff}$). The grating period is selected based on the principle that light inputted from both the left and right sides can seamlessly cover as large a field of view (FOV) as possible, while minimizing the number of diffraction orders within the operational wavelength range of our tunable laser source. As illustrated in Fig. S1(a), a planar silicon grating with a 1-μm-thick SiO_2 cladding layer generates multiple diffractive orders (Bragg period ~0.6 μm). We simulated the far fields of gratings with different periods (duty cycle $\eta = 0.5$) fed with different wavelengths. When two lights from the tunable laser (1480~1640 nm) are input from both the left and right sides, the multiple diffracted beams effectively cover a broader FOV, as depicted in Figs. S1(b)~(f). With the period $\Lambda_x = 2.16$ μm (Fig. S1(e)), the FOV is 180°, but the intersection wavelengths between different diffraction orders are close to the edge of the wavelength range. Meanwhile, with the period $\Lambda_x = 2.7$ μm (Fig. S1(f)), diffraction orders +3 through +5 and −3 through −5 can theoretically cover a 180° FOV in a wavelength range of 125 nm.

Here, the powers of different diffraction orders are not equal, whereas the Dammann grating can radiate diffraction orders of equal power. However, no literature discussion on surface-emitting silicon-based gratings exists. To make the diffracted light equally distributed to diffraction orders 3~5, we simulated a Dammann grating with a width W = 0.5 um and optimized each inversion point of the Dammann grating using a particle swarm optimization (PSO) algorithm. To guarantee a large and uniform power distribution of the outgoing beams, we defined the figure of merit (*FoM*) as

$$FoM = avg\left(P_i\right) - \sigma\left(P_i\right), \tag{S1}$$

where P_i is the power of diffraction orders 3~5, avg is the mean function, and σ is the standard deviation function. Fig. S2(b) illustrates that after 300 iterations, the FoM converges to 5.46655×10^{-7}. As shown in Figs. S2(c), the powers of diffraction orders 3~5 in the optimized Dammann grating are uniform in a wavelength range of 160 nm, and the optimized positions of the inverse points are given in Table S1.

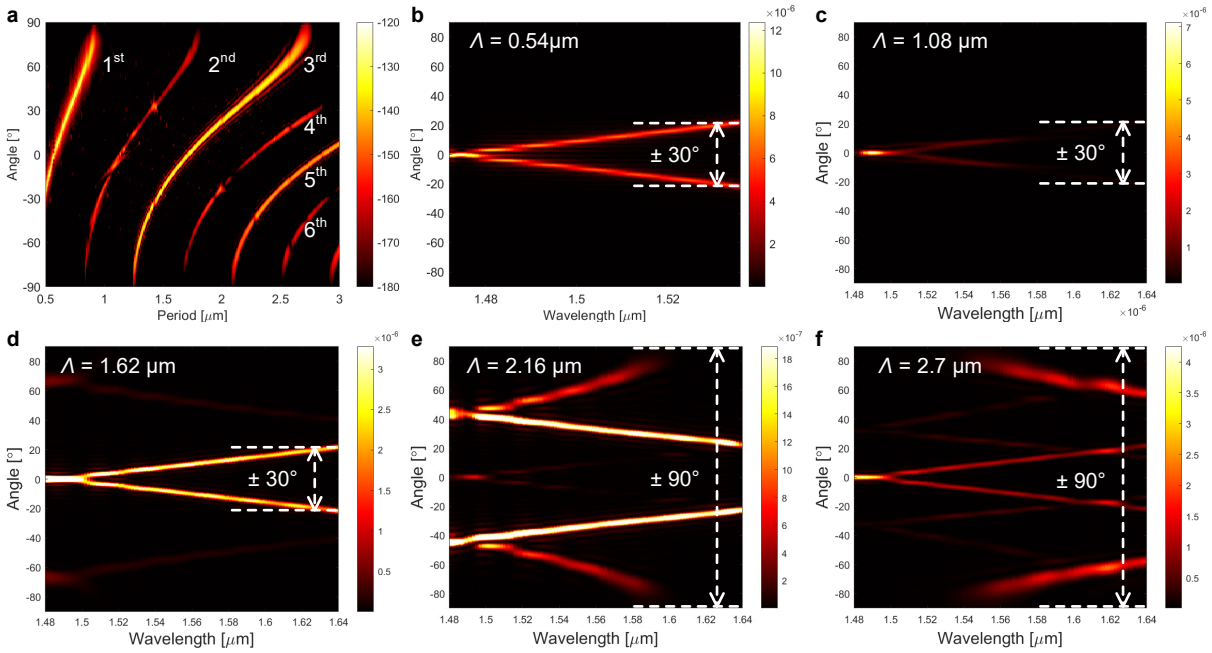

Fig. S1 (**a**) Simulated far fields $10\log|E|^2$ of the grating with varying periods ranging from 0.5 μm to 3 μm. (b)~(f)**,** Simulated far fields with different grating periods Λ = 0.54~2.7 μm in the wavelength range of 1480~1640 nm.

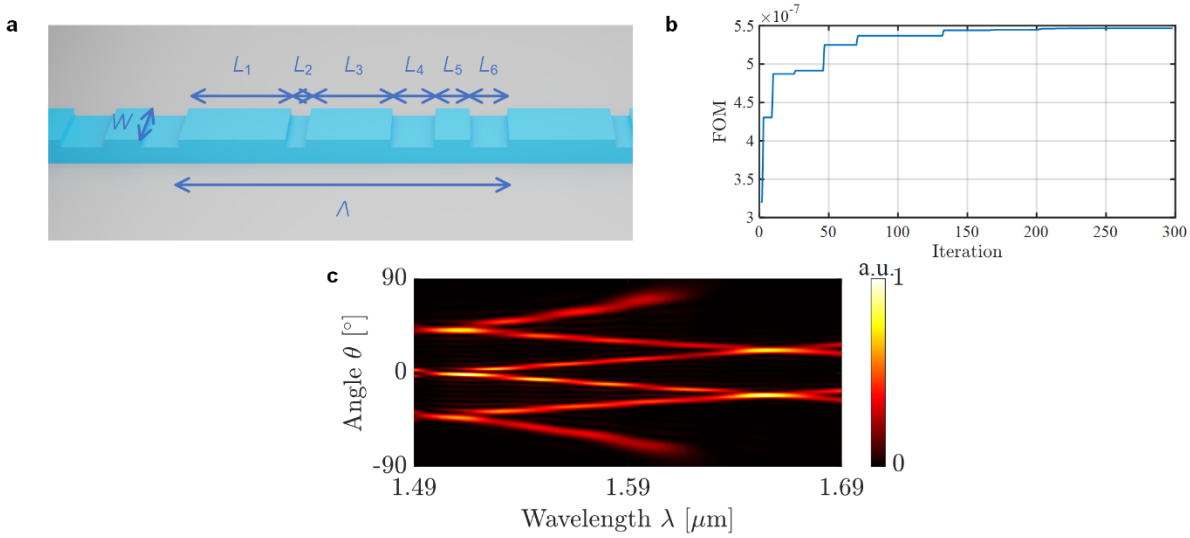

Fig. S2 (a) Three-dimensional schematic of the Dammann grating. (b) *FoM* vs. iteration in the PSO. (c) Far fields of the optimized Dammann grating with dual-directional inputs.

Table S1 Structural parameters of the optimized 1×3 Dammann grating.

Λ	L_1	L_2	L_3	L_4	L_5	L_6
2.6 μm	0.349 μm	0.282 μm	0.305 μm	0.838 μm	0.160 μm	0.666 μm

S2 Design and optimization of the waveguide-grating directional coupler

The light intensity within a grating diminishes exponentially, typically posing no issue in grating couplers with lengths shorter than 15 μm. However, as depicted in Fig. S3(a), nearly all light (99%) is emitted into free space within the initial 35-μm-long grating, and the subsequent grating structures barely impact the far-field pattern. Extending the grating length does not proportionally scale the aperture size, limiting the numerical aperture of a vertical-radiation orbital angular momentum (OAM) grating to approximately 35 μm. Nevertheless, by compensating for the emitted light power such that the power distribution conforms to an approximately Gaussian

distribution in the grating, the aperture of the grating can be expanded. To address this aspect, we have developed a waveguide-grating directional coupler (WG-DC) structure comprising a Dammann grating and a rectangular waveguide.

The gap between the waveguide and the grating was decomposed to the trigonometric series $\sum[a_n\cos(nx)+b_n\sin(nx)]$, and coefficients a_n and b_n were optimized using the PSO algorithm in MATLAB. Note that as the structure is symmetric along the x-axis because of the requirement for bi-directional input, the antisymmetric term $b_n\sin(nx)$ can be neglected. The power in the bend waveguide and the Dammann grating can be expressed as follows:

$$\begin{aligned}\frac{dP_w}{dz} &= -j\kappa_{wg}P_g e^{i2\beta z},\\ \frac{dP_g}{dz} &= -j\kappa_{gw}P_w e^{-i2\beta z-\alpha z},\end{aligned} \tag{S(2)}$$

where P_w and P_g represent the optical powers in the waveguide and grating, respectively, and κ_{wg} and κ_{gw} denote the coupling efficiencies between the waveguide and the grating. In the phase-matched DC structure, the propagation constant β in the waveguide is equal to that of the grating. The parameter α represents the attenuation coefficient of the light propagating through the grating, and its values are fitted by a 25-μm-long Dammann grating simulation in FDTD, as outlined in **Section S3**.

Here, to ensure that the power distribution in the grating closely resembles a Gaussian distribution, we define the *FoM* as follows

$$FoM = 1-\mathrm{XCorr}\left(P(x), f\left(x\,|\,\mu,\sigma\right)\right), \tag{S(3)}$$

where XCorr represents the normalized cross-correlation of two discrete sequences, and $f(x|\mu,\sigma)$ represents the normal distribution with $\mu = L_{\mathrm{grating}}/2$ and $\sigma = L^2_{\mathrm{grating}}/16$. The gap parameters, a_n, converge to the same value sets after 10 rounds of 200 iterations each in the PSO algorithm, as

shown in Fig. S3(b). The obtained WG-DC structure is depicted in Fig. S3(c). When light is launched into the waveguide, the gap initially widens, leading to weaker WG coupling. However, as the waveguide and grating gradually approach each other, the WG coupling strengthens. Beyond the midpoint, the structure of the WG-DC becomes axisymmetric with respect to the *y*-axis. The power distributions at 1490, 1590, and 1690 nm are illustrated in Figs. S3(d) and S3(e). The simulated diffraction efficiencies of the devices over the wavelength range of 1490~1690 nm are as follows: 0.115833, 0.213162, 0.235019, 0.256978, and 0.196928. This trend closely follows the power data P_B at different wavelengths shown in Fig.S3(d), with slight deviations that may explain the reduced mesh accuracy of the 3D FDTD simulation. Additionally, Fig. S3(f) provides a 3D schematic of the proposed Dammann grating.

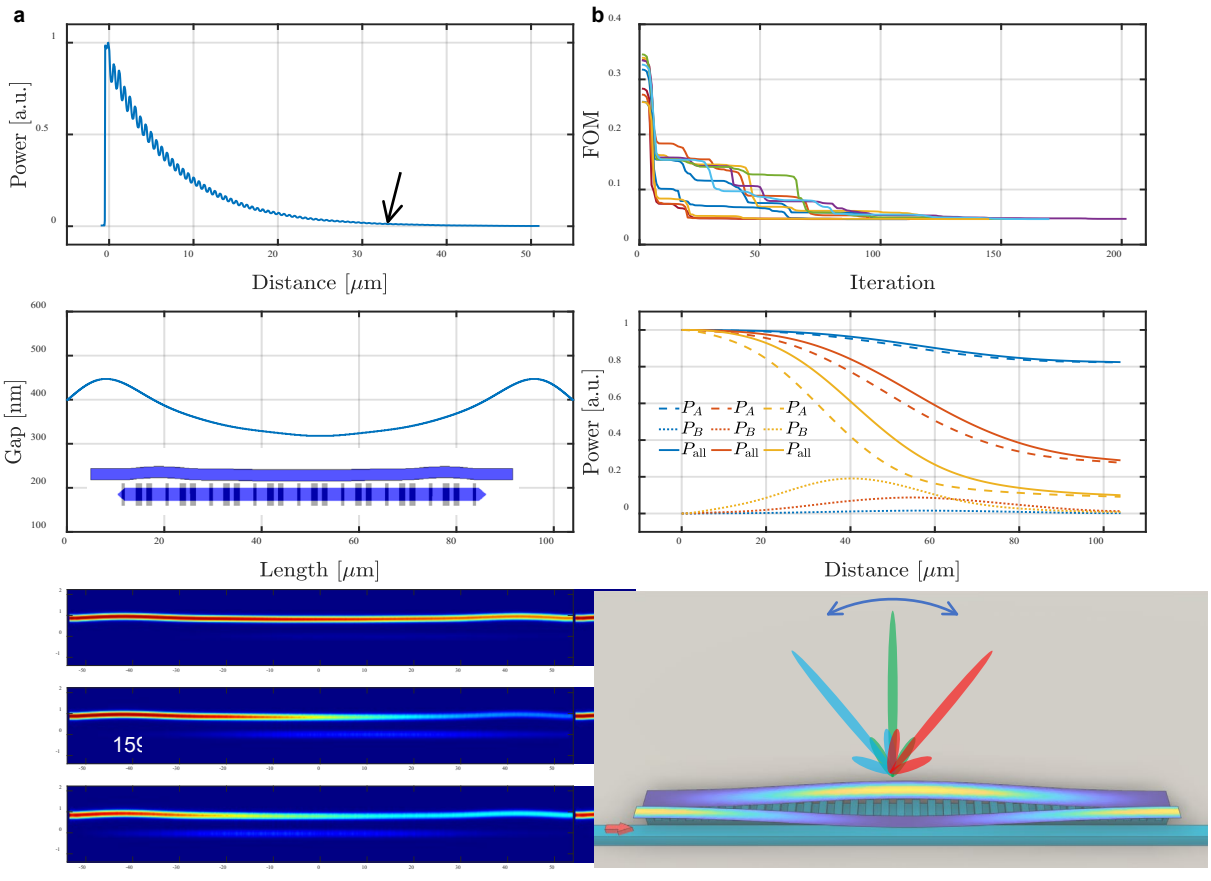

Fig. S3 Optimisation of the 1×3 Dammann grating**.** (a) 99% optical power is radiated in the first 35-μm long 70-nm shallow-etched grating. (b) All 10 PSO algorithms converge to the same FOM and parameters. (c) Gap vs. propagation direction and the top view of the WG-DC structure. (d) and (e)**,** Calculated and simulated optical powers in Dammann grating and the waveguide for three wavelengths, respectively. (f)**,** Three-dimensional schematic of the optical power distribution in the WG-DC structure for left input.

S3 Fitting of the attenuation coefficient in the Dammann grating

To acquire the attenuation coefficients of the grating at various wavelengths, we performed simulations using a 25-μm-long Dammann grating in the finite-difference time domain (FDTD) (Fig. S4(a)). The mode source was transverse electric (TE) light, and nine power monitors were strategically placed every other period (2.6 μm) to collect transmittance data over distance (Fig. S4(b)). The transmission values were fitted to the function $y = Ae^{\alpha x}$, and the resulting attenuation coefficients at different wavelengths are presented in Table S2.

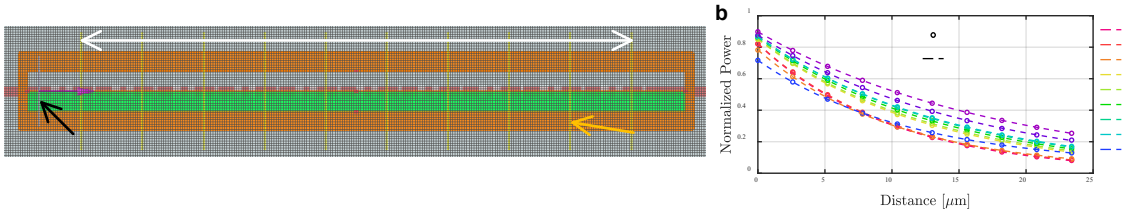

Fig. S4 (a) Setup of the proposed Dammann grating in the FDTD simulation. (b) Transmissions at various distances in the Dammann grating for the wavelength range of 1490–1690 nm and their corresponding fitted curves.

Table S2 Attenuation coefficients of the proposed 1×3 Dammann grating at different wavelengths.

λ [nm]	1480	1500	1520	1540	1560	1580	1600	1620	1640
A	0.83	0.83	0.77	0.85	0.85	0.86	0.87	0.87	0.67
$\alpha\times10^4$	–9.8	–9.6	–9.6	–7.9	–7.7	–7.3	–7.0	–6.9	–8.8

S4 Fitting the far field to OAM light

The fabricated OAM-optical phased array (OPA) chip exhibits fabrication errors on each waveguide, resulting in random optical phases for the 56 lights input into the 56 gratings. Consequently, the far-field pattern is disorganized rather than forming a clear donut shape, as shown in Fig. S5(a). To address this issue, we utilized 56 thermal phase shifters to adjust the light phase in each waveguide, ensuring that their relative phase difference was zero. Although aligning the far-field spot to maximize the power of the spot is a straightforward approach in conventional OPA, this method is not feasible for OAM light. We developed a method to fit the theoretical field distribution from the far-field spot to the OAM light. By minimizing the difference between the far-field spot and the theoretical donut shape, the phases of the lights in the input waveguides can be aligned. The proposed algorithm initially employs a genetic algorithm (GA), and after 50 iterations, gradient descent (GD) methods are utilized for fine optimization. The forked grating diffracts OAM light in the Laguerre-Gaussian mode, defined as

$$\begin{aligned} \mathrm{LG}_{p\ell}\left(r,\varphi,z\right) &= \frac{C_{p\ell}}{\omega_0}\left(\frac{\sqrt{2}r}{\omega_z}\right)^{\ell} \mathrm{L}_p^{|\ell|}\left(\frac{2r^2}{\omega\left(z\right)^2}\right)\exp\left(-\frac{r^2}{\omega\left(z\right)^2}\right)\exp\left(i\ell\varphi\right)\exp\left(i\Phi\right) \\ \Phi &= \left(\ell+2p+1\right)\arctan\frac{z}{f}-k\left(z+\frac{r^2}{2R}\right) \end{aligned} \tag{S(4)}$$

where C_{pl} is a constant, ω_0 is the waist radius, $L_p^{|\ell|}(x)$ represents the generalized Laguerre polynomials, and p and l are the radial and angular-momentum quantum numbers, respectively. Assuming that $p = 0$, and thus $L_0^{|l|}(\varsigma) = 1$, the power distribution of the vortex is

$$\mathrm{LG}_{\ell}\left(r,\varphi,z\right) = \left|\frac{C_{\ell}}{\omega_0}\left(\frac{\sqrt{2}r}{\omega_z}\right)^{\ell}\exp\left(-\frac{r^2}{\omega\left(z\right)^2}\right)\exp\left(i\ell\varphi\right)\exp\left(i\Phi\right)\right|^2 \tag{S(5)}$$

Converting Eq. S(5) into Cartesian coordinates yields

$$\mathrm{LG}_{\ell}\left(x,y,\varphi\right)=\left|\frac{C_{\ell}}{\omega_0}\left(\frac{\sqrt{2\left(x^2+y^2\right)}}{\omega_0}\right)^{\ell}\exp\left(-\frac{x^2+y^2}{\omega_0^2}\right)\right|^2$$
$$=\left|\frac{C_{\ell}}{\omega_0}\left(\frac{\sqrt{2\left(\left(x+x_0\right)^2+\left(y+y_0\right)^2\right)}}{\omega_0}\right)^{\ell}\exp\left(-\frac{\left(x+x_0\right)^2+\left(y+y_0\right)^2}{\omega_0^2}\right)\right|^2 \quad \text{S(6)}$$

Four parameters are fitted in MATLAB, namely C_{ℓ}, ω_0, x_0, and y_0. As illustrated in Fig. S5, after 100 generations of GA and GD optimization, the initially randomly distributed far field of OAM_{+4} was successfully aligned to a donut shape. We conducted far-field measurements and optimization for all lights in the wavelength range of 1505~1625 nm with all positive topological charges (left input) within ±20°.

Given the symmetry of the far field of the Dammann grating from both the left and right inputs, we only measured the far fields with negative topological charges and the far fields for the right input with an emission angle φ of 0°.

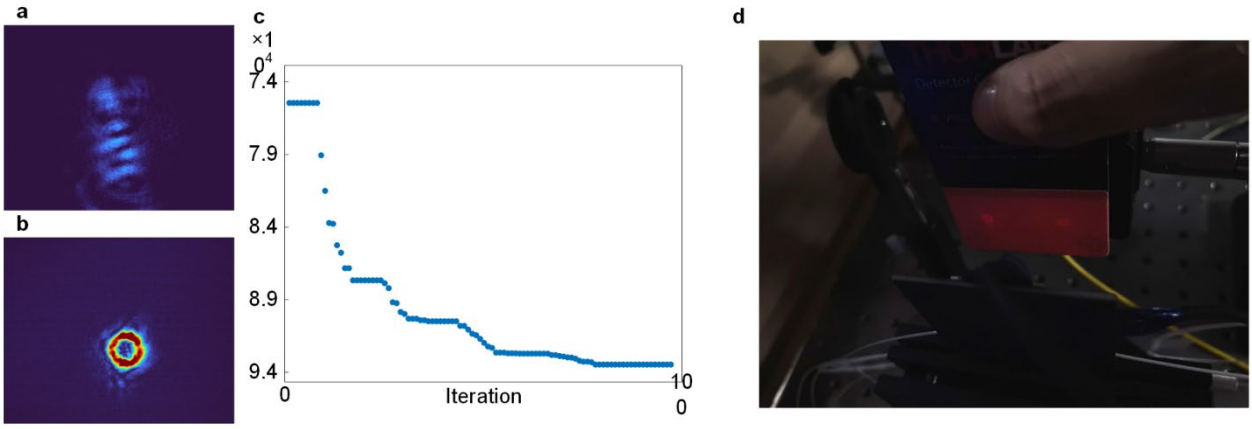

Fig. S5 (a) and (b) Initial far-field patterns before and after phase alignment, respectively. The aligned far field exhibits a donut shape, indicating successful phase alignment. (c) R^2 vs. iteration in the GA optimization. (d) With a 17dBm output power of the laser, two donut-shaped spots (OAM_3 and OAM_4) can be observed using a NIR detector card.

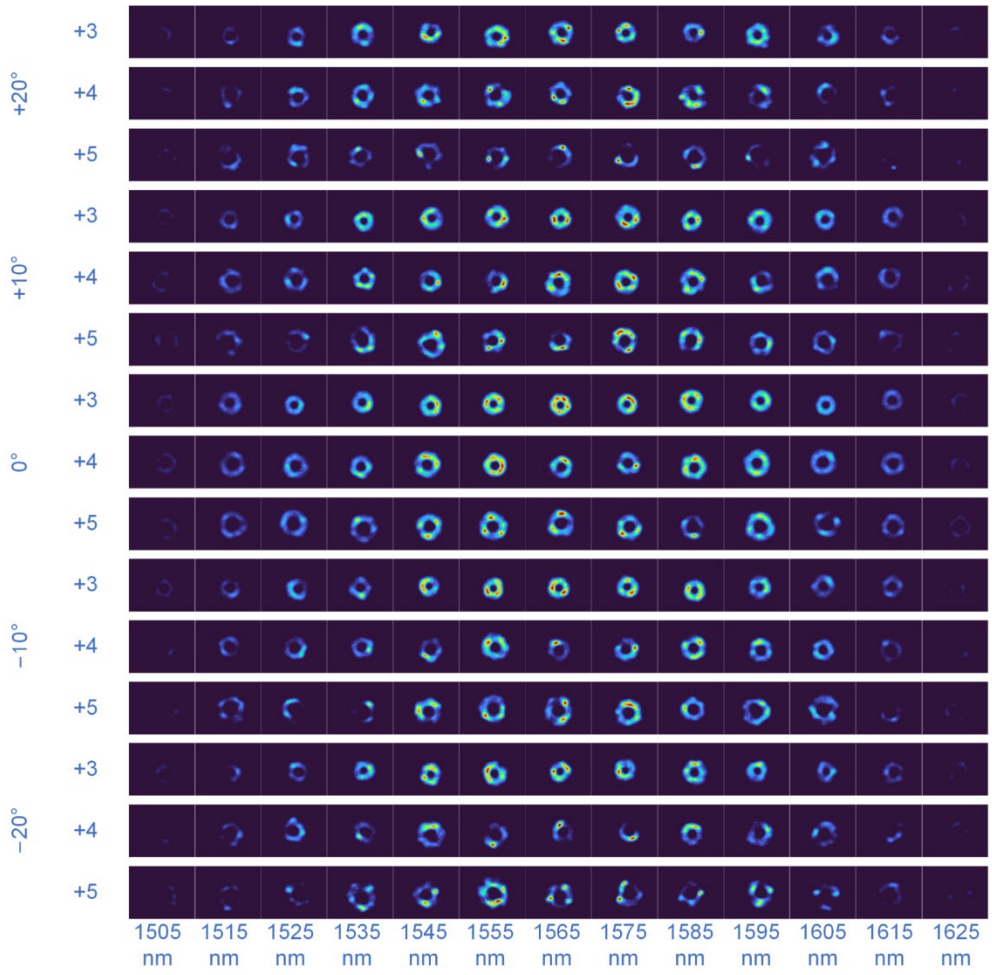
+20°
+10°
0°
−10°
−20°
+3
+4
+5
1505 nm
1515 nm
1525 nm
1535 nm
1545 nm
1555 nm
1565 nm
1575 nm
1585 nm
1595 nm
1605 nm
1615 nm
1625 nm

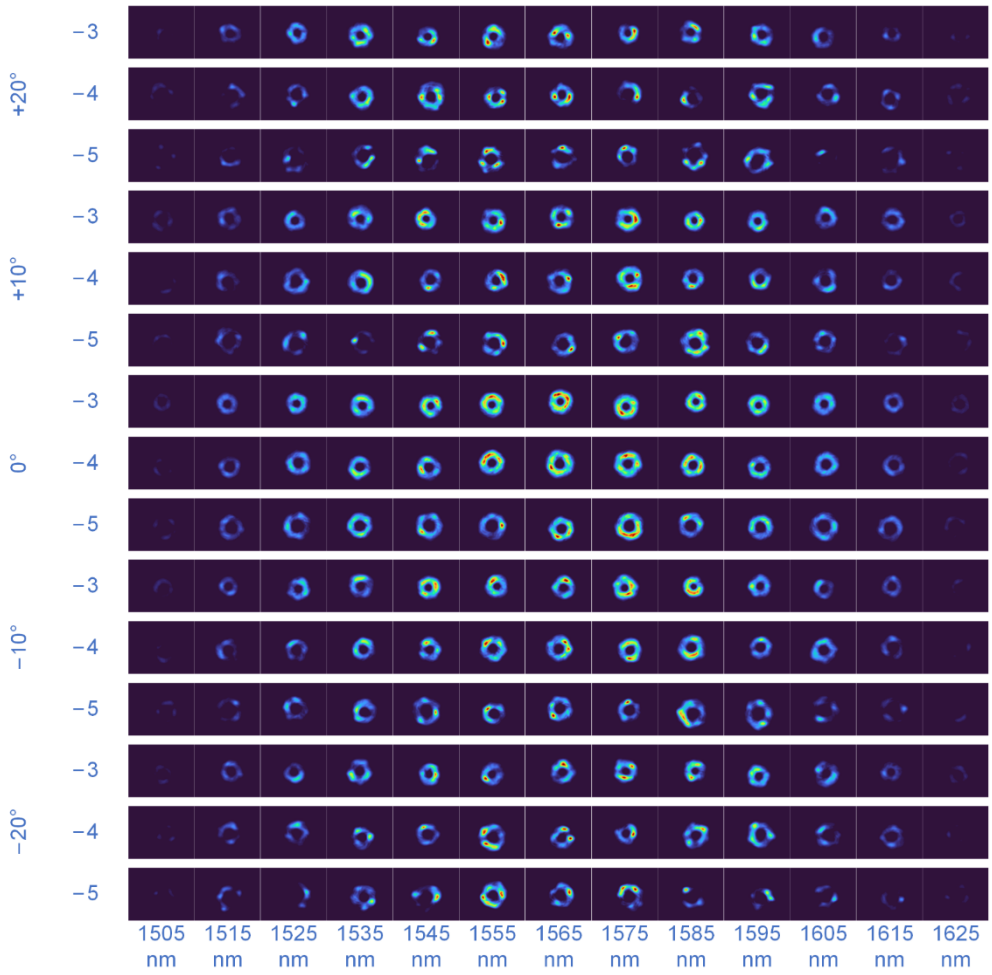

Fig. S6 Measured far fields of the $OAM_{\pm3}$, $OAM_{\pm4}$, and $OAM_{\pm5}$ with emission angles φ of −20°, −20°, 0°, +10°, and +20°.

S5 Simulations and fabrication of other silicon devices

We also conducted simulations on other silicon-based components incorporated into the OPA chip. As illustrated in Fig. S7, the results indicate that the insertion losses for the 1×2 MMI and the edge coupler are lower than 0.5 dB and 2.9 dB, respectively, across the wavelength range of 1480~1680 nm. Additionally, scanning electron microscopy (SEM) images of these silicon devices are presented in Figs. S7(e) and S7(f), providing a detailed visual representation.

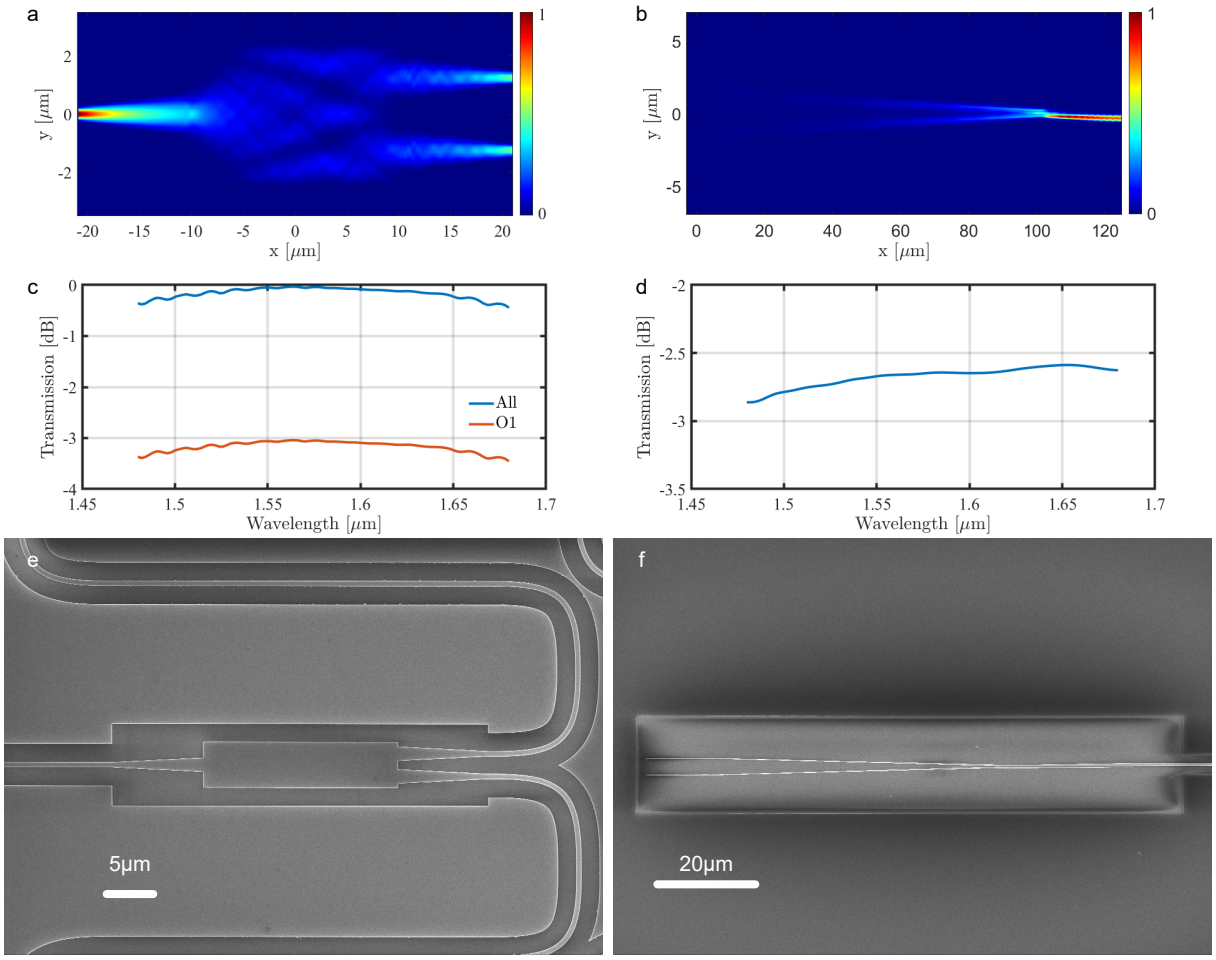

Fig. S7 Simulated power distributions, transmission, and SEM images of 1×2 MMI and forked edge coupler.